

Article

Hydrazine High-Performance Oxidation and Sensing Using a Copper Oxide Nanosheet Electrocatalyst Prepared via a Foam-Surfactant Dual Template

Etab M. Almutairi , Mohamed A. Ghanem * , Abdulrahman Al-Warthan , Mufsir Kuniyil  and Syed F. Adil 

Chemistry Department, College of Science, King Saud University, Riyadh 11451, Saudi Arabia

* Correspondence: mghanem@ksu.edu.sa; Tel.: +966-114670405; Fax: +966-14675992

Abstract: This work demonstrates hydrazine electro-oxidation and sensing using an ultrathin copper oxide nanosheet (CuO-NS) architecture prepared via a versatile foam-surfactant dual template (FSDT) approach. CuO-NS was synthesised by chemical deposition of the hexagonal surfactant Brij[®]58 liquid crystal template containing dissolved copper ions using hydrogen foam that was concurrently generated by a sodium borohydride reducing agent. The physical characterisations of the CuO-NS showed the formation of a two-dimensional (2D) ultrathin nanosheet architecture of crystalline CuO with a specific surface area of ~ 39 m²/g. The electrochemical CuO-NS oxidation and sensing performance for hydrazine oxidation revealed that the CuO nanosheets had a superior oxidation performance compared with *bare*-CuO, and the reported state-of-the-art catalysts had a high hydrazine sensitivity of 1.47 mA/cm² mM, a low detection limit of 15 μ M (S/N = 3), and a linear concentration range of up to 45 mM. Moreover, CuO-NS shows considerable potential for the practical use of hydrazine detection in tap and bottled water samples with a good recovery achieved. Furthermore, the foam-surfactant dual template (FSDT) one-pot synthesis approach could be used to produce a wide range of nanomaterials with various compositions and nanoarchitectures at ambient conditions for boosting the electrochemical catalytic reactions.



Citation: Almutairi, E.M.; Ghanem, M.A.; Al-Warthan, A.; Kuniyil, M.; Adil, S.F. Hydrazine

High-Performance Oxidation and Sensing Using a Copper Oxide Nanosheet Electrocatalyst Prepared via a Foam-Surfactant Dual Template. *Nanomaterials* **2023**, *13*, 129. <https://doi.org/10.3390/nano13010129>

Academic Editors: Xuezhi Song and Emmanuel Iwuoha

Received: 15 November 2022

Revised: 22 December 2022

Accepted: 23 December 2022

Published: 26 December 2022



Copyright: © 2022 by the authors. Licensee MDPI, Basel, Switzerland. This article is an open access article distributed under the terms and conditions of the Creative Commons Attribution (CC BY) license (<https://creativecommons.org/licenses/by/4.0/>).

Keywords: surfactant; foam; dual templates; copper oxide; nanosheets; hydrazine sensing

1. Introduction

According to recent reports, the global production of hydrazine (diamine, N₂H₄) and its derivatives reaches up to 200,000 metric tons a year [1], and it is widely used in explosives and fuels [2], particularly rocket fuel [3]. Moreover, recently, hydrazine has been used in an enormous range of industrial applications, such as corrosion inhibitors [4], reducing agents [5], photographic chemicals [6], drug production [7,8], antioxidants [9], and herbicides [10]. However, the spread of hydrazine usage has increased environmental pollution because it is classified as a highly toxic substance [11]. It has been declared carcinogenic as it can damage the brain, liver, and eyes when absorbed from the metabolized drug or the environment [12,13]. In addition, it has been classified as a B2 group environmental pollutant by the Environmental Protection Agency (EPA) and World Health Organisation (WHO) [14]. Therefore, it is necessary to measure the hydrazine concentration in different types of samples, particularly in aqueous systems.

Several analytical methods, such as chromatography [15], fluorescence methods [16], chemiluminescence [17], and electrochemical methods [18], have been used for the detection of hydrazine in various types of samples. Among these methods, electrochemical techniques are considered to be the best because of their simplicity, low-cost fabrication process, and fast detection response, and because they possess a relatively high sensitivity and selectivity [19–21]. However, electrochemical methods with conventional substrates usually show a lower sensitivity and selectivity for sample analysis than electrochemical methods based on a modified electrode [22,23]. Therefore, it is necessary to develop more efficient

modified electrodes to achieve the detection of low limits, eliminate interferences, and improve the electrochemical sensing results. Hence, transition-metal oxides and hydroxide nanomaterials of cobalt, nickel, and copper have attracted extensive research attention in recent years for the development of an electrochemical hydrazine sensing platform because of advantages such as a high catalytic activity, low cost, environment friendliness, good stability, and ease of manufacturing and developing electrochemical sensors [24,25].

In particular, among the transition metal oxide nanostructures, copper oxide (CuO) is one of the known p-type semiconductor materials with a narrow band gap of 1.2 eV; it offers interesting photovoltaic, photoconductive, and electrocatalytic properties [26–30]. Many new CuO-based nanoarchitectures with a high specific surface area and mesoporosity, various morphologies, and compositions have shown a significant enhancement in sensor [31–33] and electrochemical energy reaction [34,35] applications. For example, CuO nanoparticles [36], nanowires [37], nanoflakes [38], nanoflowers [39], nanosheets, and microspheres [25,40] have been developed for catalysing hydrazine sensing and have shown unique advantages over traditional sensors. In particular, two-dimensional (2D) copper oxide nanosheet architectures have shown a significant hydrazine oxidation activity because of their shortened ion and electron diffusion pathways, an abundance of mesoporous channels and active sites for catalysts, excellent mechanical properties, and improved structural stability [40–42].

Several synthesis methods such as hydrothermal routes [43,44], chemical bath deposition methods (CBD) [45], spray pyrolysis [46], microwave irradiation [47], and sol–gel [48] have been reported for the preparation of CuO-NS and their application as sensing electrodes. Considerable focus has been on chemical methods that allow one to control the morphology and particle size, as there is evidence that particle size and morphology directly affect the properties of the catalysts [49,50]. This has been accomplished by considering several synthesis factors such as the type of surfactant template, solvents, temperature, and reactant concentration [40,51]. Recently, the soft-template approach as the chemical method has been widely exploited because of its one-step route that produces high-surface-area mesoporous nanostructured compounds [52–54]. Using this approach, our research group reported a foam-surfactant dual template (FSDT) approach to produce mesoporous Ni/Ni(OH)₂ 2D nanoarchitecture (nanoflakes) via chemical deposition from a hexagonal lyotropic surfactant template using a sodium borohydride reducing agent [55]. The Ni/Ni(OH)₂ nanoflake catalyst has shown substantial enhancement of the electrochemical nature of methanol and urea oxidation and glucose sensing reactions [51]. Naikoo et al. successfully synthesised macro/mesostructured porous copper oxide via a facile and environmentally benign soft template method by controlling the parameters of shape, dimensionality, and crystallinity. The obtained results revealed that mesoporous copper oxide materials have an excellent catalytic activity towards the oxidation of phenol because of their unique porous nature [56].

To improve the synthesis of CuO nanostructures and further explore their unique properties, the present work, for the first time, demonstrates a novel chemical deposition of 2D CuO nanosheet architecture at room temperature using the versatile foam-surfactant dual templates (FSDT) of self-assembled Brij[®]58 surfactant liquid crystal template and in situ hydrogen foam exfoliation produced by a sodium borohydride (NaBH₄) reducing agent. A thin layer of Brij[®]58 surfactant mixed with a copper nitrate solution was firstly self-assembled in a Petri dish and an excess of NaBH₄ solution addition was followed. The copper ions confined in the aqueous domain of the template were reduced by NaBH₄ and the in situ foam of hydrogen bubbles concurrently exfoliated the deposited CuO nano-layers. The physicochemical characterisation of the CuO nanosheet crystal structure and nanostructured morphology were performed using X-ray diffraction, N₂ adsorption-desorption isotherms, X-ray photoelectron spectroscopy, and scanning and transmission electron microscopy. The electrochemical hydrazine oxidation and sensing performance at the CuO nanosheet electrode in an alkaline solution was examined by electrochemical and impedance techniques, and evaluated against that of the *bare*-CuO that was deposited

without the surfactant and was compared with the state-of-the-art copper-based-catalysts reported thus far.

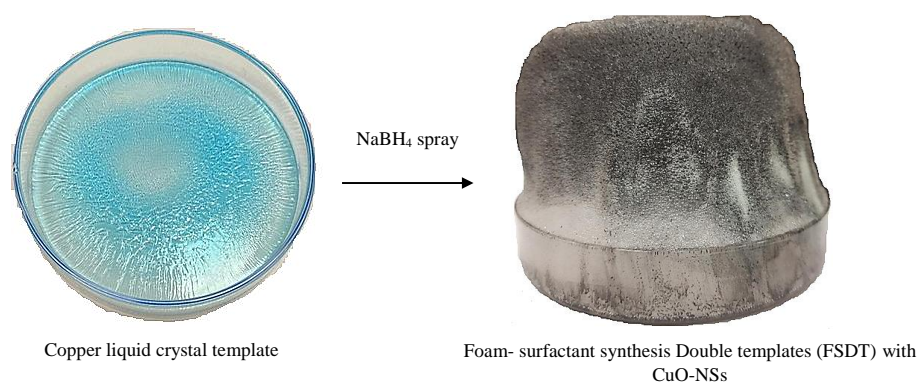
2. Materials and Methods

2.1. Materials and Chemicals

Copper (II) nitrate trihydrate $\text{Cu}(\text{NO}_3)_2 \cdot 3\text{H}_2\text{O}$, the (Brij[®]58) polyethylene glycol octadecyl ether, hydrazine 80%, uric acid (UA), sodium chloride (NaCl), cysteine, sodium borohydride, NaBH_4 , and Nafion (5% in a mixture of water and lower aliphatic alcohols), were purchased from Sigma Aldrich (Dorset, UK). Isopropanol (>99%) was procured from WINLAB (Leicester, UK) and potassium hydroxide (KOH, 85%, pellets) was bought from LOBA Chemie (Mumbai, India). All of the solutions in the experiment were prepared using deionized water obtained from a Milli-Q ultrapure water purification system. Real samples were obtained from Nova Company (Riyadh, KSA) and using tap water from the laboratory.

2.2. Synthesis of CuO Nanosheets (CuO-NS)

The CuO nanosheet catalyst was prepared at room temperature (25 °C) using the approach of the foam-surfactant dual template (FSDT) employing the reducing agent of sodium borohydride (NaBH_4). In the FSDT approach, the copper ions confined in the intestinal aqueous domain of the Brij@58 hexagonal LCT are chemically reduced by the NaBH_4 , which concurrently produces foam of hydrogen bubbles that simultaneously exfoliate and scale off the deposited catalyst layers [51,55]. In brief, as shown in Scheme 1, the copper liquid crystal template (Cu-LCT) mixture was prepared by physically adding 5.0 g of a 0.5 M copper (II) nitrate solution, 2.0 g of the melted non-ionic Brij[®]58 surfactant, and 5.0 g of distilled water in a glass beaker. Using an ultrasonic probe, the template mixture was sonicated until a homogenous solution was obtained (15.0 min) and then transferred to a Petri dish. Then, the surfactant to water ratio was adjusted at 40% via evaporation of the excess water in an open atmosphere at 25 °C to form a thin layer of hexagonal liquid crystal copper template. Then, the gel template in the Petri dish was sprayed with an excess of sodium borohydride (1.0 M) reducing agent. After a few seconds, as shown in Scheme 1, excessive hydrogen bubble effervescence and foam were formed, and the copper template mixture changed to black, indicating the reduction of copper ions confined in the liquid crystal template.



Scheme 1. The foam-surfactant dual template synthesis (FSDT) synthesis approach of CuO-NNs using a sodium borohydride (NaBH_4) reducing agent.

2.3. Characterisation of CuO Nanosheets

The crystal structure and the surface composition of the as-synthesised CuO nanosheets and *bare*-CuO were analysed by X-ray diffraction (XRD, D2 Phaser Bruker (Berlin, Germany) fitted with Cu $K\alpha$ radiation ($\lambda = 1.5418 \text{ \AA}$), and an X-ray photoemission spectroscopy analysis was conducted with an Escalab 250 spectrometer (XPS) from Thermo Fisher Scientific

(Oxford, UK). The CuO nanosheets' and *bare*-CuO catalysts' morphology and nanoarchitecture were analysed using a scanning (SEM, JSM-7600F; JEOL, Tokyo, Japan) and transmission electron microscope integrated with an electron diffraction (SAED) analysis unit (TEM, JEM 2100F-JEOL, Tokyo, Japan), separately. The specific surface area and the porosity of the CuO nanosheets were determined with a V-Sorb 2800 Porosimetry Analyser (Microtrac Retsch, Haan, Germany) using the Brunauer–Emmett–Teller (BET) technique.

The cyclic voltammetry (CV), chronoamperometry (CA), and impedance (EIS) analysis electrochemical characterisations techniques were performed using the Metrohm AutoLab (PGSTAT302N, Utrecht, Netherlands) Potentiostatic/Galvanostat. A three-electrode electrochemical cell was used for the electrochemical measurements with a platinum sheet ($0.5 \times 0.5 \text{ cm}^2$) and Ag/AgCl as a counter and reference electrode, respectively. The working electrode was made of carbon paper (CP, SIGRACET® GDL 24BC, $1.0 \text{ cm} \times 1.0 \text{ cm}^2$) modified with catalyst ink and the KOH solution as the electrolyte. For the electrochemical characterisation, the ink of the CuO nanosheets was obtained by sonicating 10 mg of the CuO-NS or *bare*-CuO catalyst, 10 μL of Nafion, 0.5 mL of isopropanol, and 0.5 mL of deionized water in a glass vial for 30 min using an ultrasonication probe.

3. Results and Discussion

3.1. Characterisation of the CuO Nanosheet Structure

The crystal structure and purity of the as-prepared CuO nanosheets were investigated using X-ray diffraction (Cu-K α radiation). Figure 1a shows the XRD pattern, which reveals the orientation and crystalline nature of the copper oxide nanosheets. The peaks located at 2θ values of 31.90° , 35.21° , 38.5° , 48.53° , 53.29° , 58.07° , 61.25° , 65.90° , 67.82° , 72.17° , and 74.87° were indexed as the (110), (002), (111), (202), (020), (202), (113), (022), (310), (311), and (222) planes, respectively. The above-mentioned diffraction peaks were matched well with the crystalline monoclinic crystal structure of CuO (ICSD:98-006-9757). These results indicate that the synthesised CuO nanosheets were in their pure form and free of any impurities. Moreover, the average size of the CuO nanosheets estimated from the XRD profile and using Debye–Scherrer's equation was found to be 10.36 nm [27,29]. The XRD of the *bare*-CuO in Figure S1 showed similar results, which indicate that the surfactant use did not affect the CuO crystal structure growth.

Figure 1b shows the N₂ adsorption and desorption isotherms, as well as the pore size distribution curves (inset) of the *bare*-CuO and CuO-NS catalysts. The adsorption–desorption isotherm curve of the CuO-NS catalyst revealed typical type IV isotherms with a hysteresis loop of type H₁ in the p/p^0 region of 0.4–1.0, which could be attributed to the N₂ gas capillary condensation within the mesoporous structure and the slit pores in-between the nanosheets, indicating that the catalysts had a mesoporous architecture [57].

Moreover, the N₂ isotherm showed that the *bare*-CuO exhibited a very narrow hysteresis loop with a smaller surface area ($20.55 \text{ m}^2/\text{g}$), while CuO-NS had wider hysteresis and a higher capillary uptake at a lower pressure and specific surface area ($39.42 \text{ m}^2/\text{g}$), thus signifying the presence of higher mesoporosity. In addition, as shown in the inset of Figure 1b, the pore size distribution curve obtained by the BJH method further confirmed the development of many irregular mesopores within the range of 10–70 nm in the case of the CuO-NS catalyst.

The composition and surface functionality of the as-prepared CuO-NSs were further investigated by XPS analysis. The survey spectrum in Figure S1 reveals the main elemental composition of the O 1s and Cu 2p peaks, in addition to that of the C 1s originating from the background and/or the surfactant contamination [58,59]. As shown in Figure 1c, the narrow deconvoluted core spectra of Cu 2p showed that the peaks located at 934.9 eV and 954.3 eV could be assigned to Cu 2p_{3/2} and Cu 2p_{1/2}, respectively [57,58]. The binding energy separation between the Cu 2p_{3/2} and the Cu 2p_{1/2} peaks was 19.9 eV, which is characteristic of CuO. Meanwhile, the intense satellite features at 943.2 eV and 963.1 eV could be ascribed to the Cu 2p_{3/2} and Cu 2p_{1/2} in CuO, respectively. The deconvoluted core spectra of the O 1s displayed in Figure 1d shows two peaks at 531.2 and 530.1 eV. The

low binding energy peak at 530.1 eV could be attributed to the lattice oxygen within the metal oxide ($\text{CuO} = \text{O}$, 530.1 eV), whereas the high binding energy peak at 531.2 eV might be assigned to the low coordination surface oxygen species and surface oxygen defects, which could improve the intrinsic catalytic activity of the CuO catalyst [57,58].

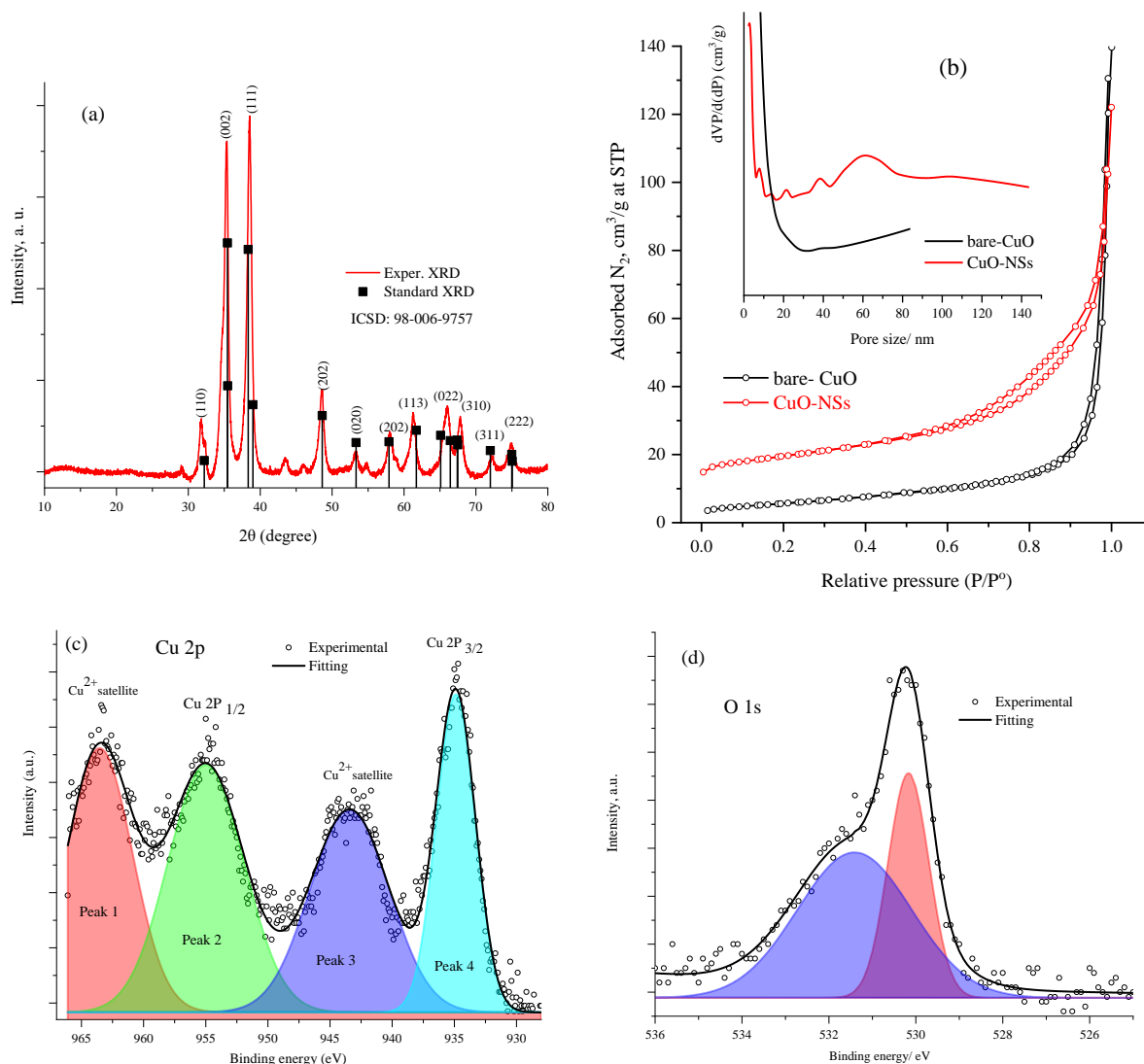


Figure 1. (a) The XRD pattern and crystalline nature of the copper oxide nanosheets, (b) the N_2 adsorption–desorption isotherms and the pore size distribution curves (inset) of the *bare*-CuO and CuO-NS catalysts, (c) the narrow XPS deconvoluted core spectra of Cu 2p, and (d) the deconvoluted XPS core spectra of the O 1s orbital.

The surface morphology of the CuO-NS catalyst was characterised using scanning electron (SEM) and transmission electron microscopy (TEM) to determine its nanoarchitecture morphology. Figure 2a,b shows the SEM images of the as-synthesised nanostructured CuO-NS taken at different magnifications, revealing the morphology of the overlapped and aggregated nanosheets, as well as the interstitial mesoporous channels with various nanostructure sizes that facilitate the mass transport diffusion of the analyte molecules. In contrast, Figure 2c shows the TEM image of CuO-NS, which confirms the 2D nanosheet morphology of the CuO catalyst. The TEM image revealed the presence of bright and dark areas, which corresponded to the individual and stacked nanosheet structures, respectively. The dark areas indicate the regions with stacking between sheets in different crystallographic directions.

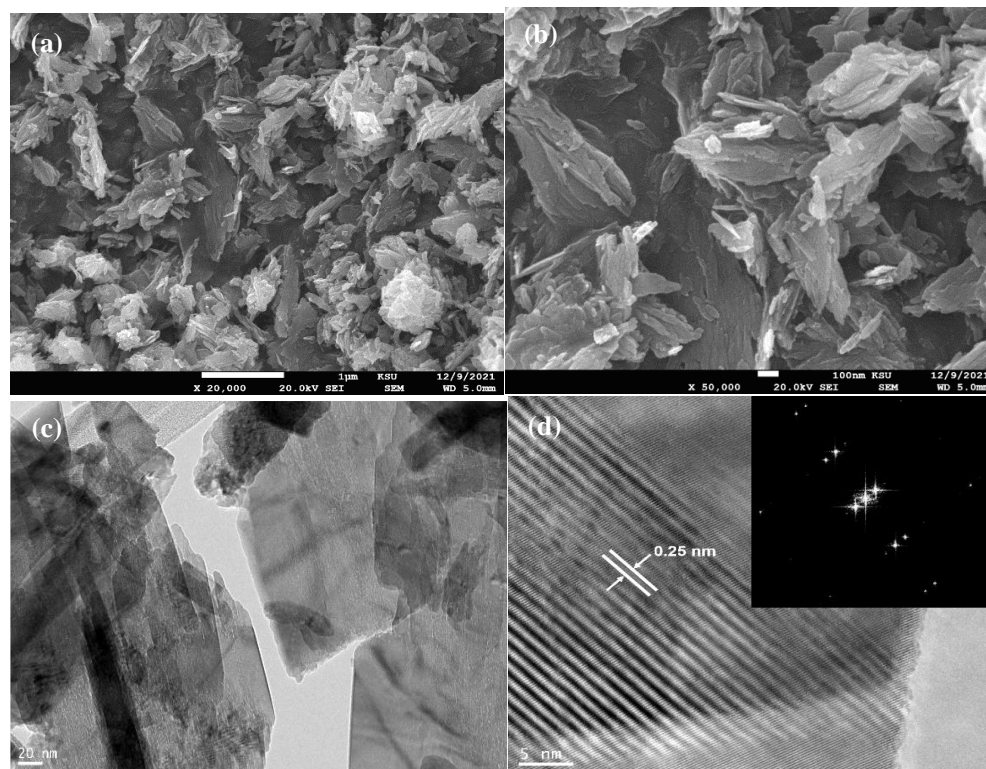


Figure 2. Surface morphology of the CuO-NS catalyst. (a,b) SEM images of the as-synthesised nanostructured CuO-NS taken at different magnifications. (c) TEM image of the CuO-NS catalyst. (d) HR-TEM of the CuO-NS lattice fringes and the inset shows the transmission electron diffraction pattern image.

The lattice fringe could be seen in the HR-TEM image shown in Figure 2d. The lattice spacing between the adjacent planes was approximately 0.25 nm, corresponding to the distance between the (111) crystal plane of the CuO diffraction pattern (ICSD:98-006-9757). Furthermore, Figure S3a shows the SAED pattern of the CuO nanosheets that reveal the presence of the lattice planes of the monoclinic CuO nanosheet crystal structure (ICSD:98-006-9757). The SAED pattern confirmed the good crystallinity of the CuO nanosheets, which was in good agreement with the XRD results. Moreover, for comparison, Figure S3b shows the TEM characterisation image of the *bare*-CuO catalyst deposited in the absence of the surfactant. The TEM image shows that the *bare*-CuO had a thick deposit of bulky micro-particles with the absence of a nanosheet morphology.

3.2. Electrochemical Characterisation of CuO-NS Electrode

The electrocatalytic activity of CuO-NS in comparison with that of the *bare*-CuO electrodes towards the hydrazine oxidation and sensing was examined using the cyclic voltammetry technique. Figure 3a shows the results of the cyclic voltammetry conducted at a scan rate of 50 mV/s and in the potential range of -0.2 to 0.8 V versus Ag/AgCl of CuO-NS in comparison with those of the *bare*-CuO loaded on the carbon paper electrode in the absence and presence of 20 mM hydrazine dissolved in 1.0 M KOH as a supporting electrolyte. In the absence of hydrazine, a very small current density was observed at the *bare*-CuO electrode (black line) up to a potential of 0.8 V versus Ag/AgCl. In contrast, the CuO-NS electrode in the absence of hydrazine showed significant current density increases around the potential of 0.6 V versus Ag/AgCl (green line), indicating the commencement of the oxygen evolution reaction at the CuO-NS catalyst in the 1.0 M KOH solution. Upon the addition of 20 mM hydrazine to the 1.0 M KOH electrolyte, the CuO-NS electrode exhibited an enormous oxidation peak (blue line) at the onset potential of -0.03 V and the peak potential of 0.35 V versus Ag/AgCl, which could be attributed to the oxidation of the

added hydrazine. The oxidation peak current reached 15.60 mA/cm^2 during the first cycle and stabilized at a slightly lower current of 14.70 mA/cm^2 during the successive cycles. In contrast, the *bare*-CuO electrode showed a considerably lower electrocatalytic response to the hydrazine oxidation at a more positive potential of 0.55 V versus Ag/AgCl (red line).

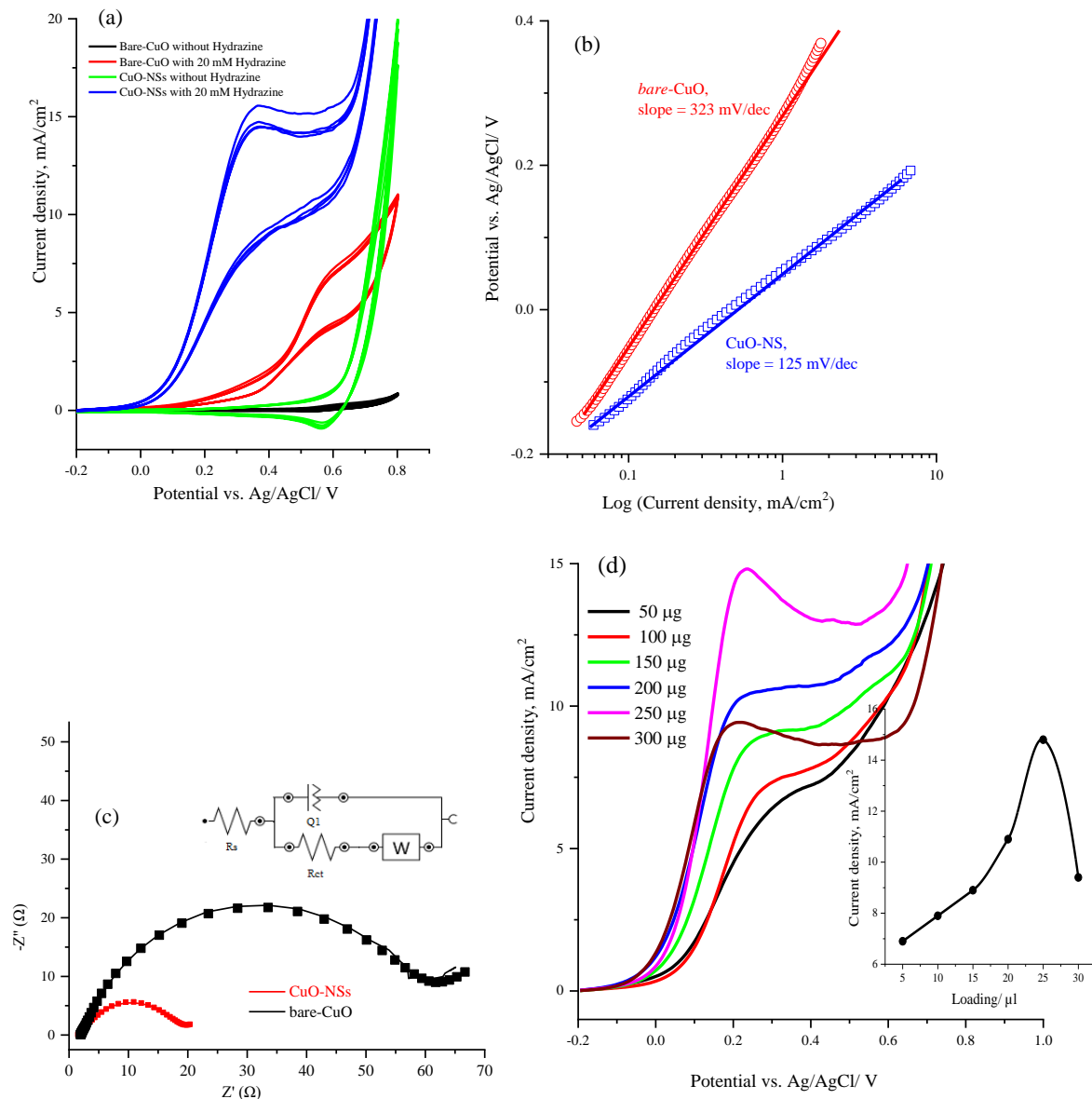


Figure 3. (a) Cyclic voltammetry at a scan rate of 50 mV/s of CuO-NS ($250 \mu\text{g}$) in comparison to those of the *bare*-CuO catalyst loaded on the carbon paper electrode in the absence and presence of 20 mM hydrazine dissolved in 1.0 M KOH solution. (b) Tafel plots of CuO-NS and *bare*-CuO electrodes obtained by fitting the corresponding linear sweep voltammetry results to the Tafel equation. (c) The Nyquist plots of the CuO-NS ($250 \mu\text{g}$) compared with *bare*-CuO-NS electrodes in the 1.0 M KOH solution containing 10-mM hydrazine at an applied potential of 0.15 V vs. Ag/AgCl and in the frequency range from 0.01 to 10^5 Hz and the inset is the fitted equivalent circuit. (d) CVs of the CuO-NS catalyst with different loadings ranging from 50 to $300 \mu\text{g}$ as recorded at 50 mV/s in 20 mM hydrazine dissolved in the 1.0 M KOH solution; the inset is the corresponding correlation between the hydrazine oxidation peak current density and the catalyst loading.

The hydrazine oxidation kinetics of the CuO-NS compared with the *bare*-CuO electrode was investigated by Tafel plots obtained by fitting the linear cyclic voltammetry results to the Tafel equation, as shown in Figure 3b. It can be noted that the Tafel slope of the CuO-NS

electrode (125 mV/dec) was significantly much lower than in the case of the *bare*-CuO electrode (323 mV/dec), which indicates much faster charge transfer kinetics and that less overpotential is required to oxidized hydrazine when using the CuO-NS electrode.

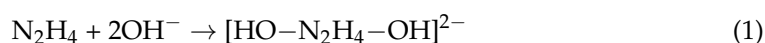
Electrochemical impedance spectroscopy (EIS) was employed to confirm the facilitation of the electron transfer kinetics at the CuO-NS electrode. Figure 3c displays the Nyquist plots of CuO-NS compared with the *bare*-CuO-NS electrodes in the 1.0 M KOH solution containing 10 mM hydrazine and in the frequency range from 0.01 to 10⁵ Hz at an applied potential of 0.15 V versus Ag/AgCl. The CuO-NS electrode exhibited a smaller diameter semicircle at a low frequency than the *bare*-CuO electrode, indicating that the CuO-NS electrode was considerably less resistive to the charge transfer. The inset of Figure 3c shows the equivalent circuit that fits the corresponding Nyquist diagrams, where R_s is the solution resistance and the R_{ct} represents the hydrazine oxidation charge transfer resistance, and Q_1 is the double electric layer capacitance of the CuO-NS electrode. The Warburg impedance (W) due to the charge transfer at the catalyst/electrolyte interface was observed in the case of the diffusion-controlled reaction. The corresponding impedance parameters obtained from the fitting circuit are reported in Table 1; it can be observed that the CuO-NS electrode showed a considerably lower R_{ct} value (8.17 Ω) than the *bare*-CuO electrode (52.72 Ω), further evidence that the charge transfer occurred considerably faster at the CuO-NS electrode.

Table 1. The equivalent circuit parameter values of the ISE spectra of hydrazine oxidation at the CuO-NSs and *bare*-CuO electrodes.

Element	CuO -NSs	<i>Bare</i> -CuO
R_s (Ω)	1.18	1.96
Q_1 (mF)	64.4	0.409
R_{CT} (Ω)	8.17	52.72
W_1 (Ω/cm^2)	0.70691	0.098586

The hydrazine oxidation catalytic current was significantly enhanced with the increase in the CuO-NS catalyst loading, and as shown in Figure 3d, the CVs of the CuO-NS catalyst with different loadings ranging from 50 to 300 μg were obtained at 50 mV/s in 20 mM hydrazine dissolved in the 1.0 M KOH solution. As shown in the inset in Figure 3d, the relationship between the hydrazine oxidation peak current density and the catalyst loading exhibited a volcanic plot with a gradual increase in the oxidation peak current as the catalyst loading increased, reaching a maximum oxidation peak current of 14.80 mA/cm² at a catalyst loading of around 250 μg . The loading effect trend could be related to the increase in the available electrochemical active sites of the CuO-NS catalyst with an increase in the catalyst loading. In addition, the decrease in the hydrazine oxidation current above a catalyst loading of >250 μg could be attributed to the retardation of the electron transfer and the active ion diffusion within the thicker catalyst film.

The cyclic voltammetry and impedance results indicate that the CuO-NS electrode showed a significant oxidation performance and faster charge transfer during the electrocatalytic hydrazine oxidation reaction compared with the *bare*-CuO electrode, which could be related to the nanosheet architecture with an enhanced surface area and electron transfer kinetics [60–63]. Based on recent studies, the mechanism of hydrazine oxidation by the electrocatalytic process significantly depends on the electrode surface nature and the electrolyte solution [60–63]. In the case of the CuO electrode in an alkaline solution, the mechanism could be proposed to proceed via the irreversible reactions of the hydrazine oxidation at the CuO electrode where the formed intermediate complex of hydrazine in Equation (1) is oxidized at the CuO-NSs surface, producing the N₂ gas as described by Equations (2) and (3).





The effect of the hydrazine concentration was also investigated using linear sweep voltammetry (LSV) at 50 mV/s, using 250 μg of the CuO-NS electrode, as shown in Figure 4a.

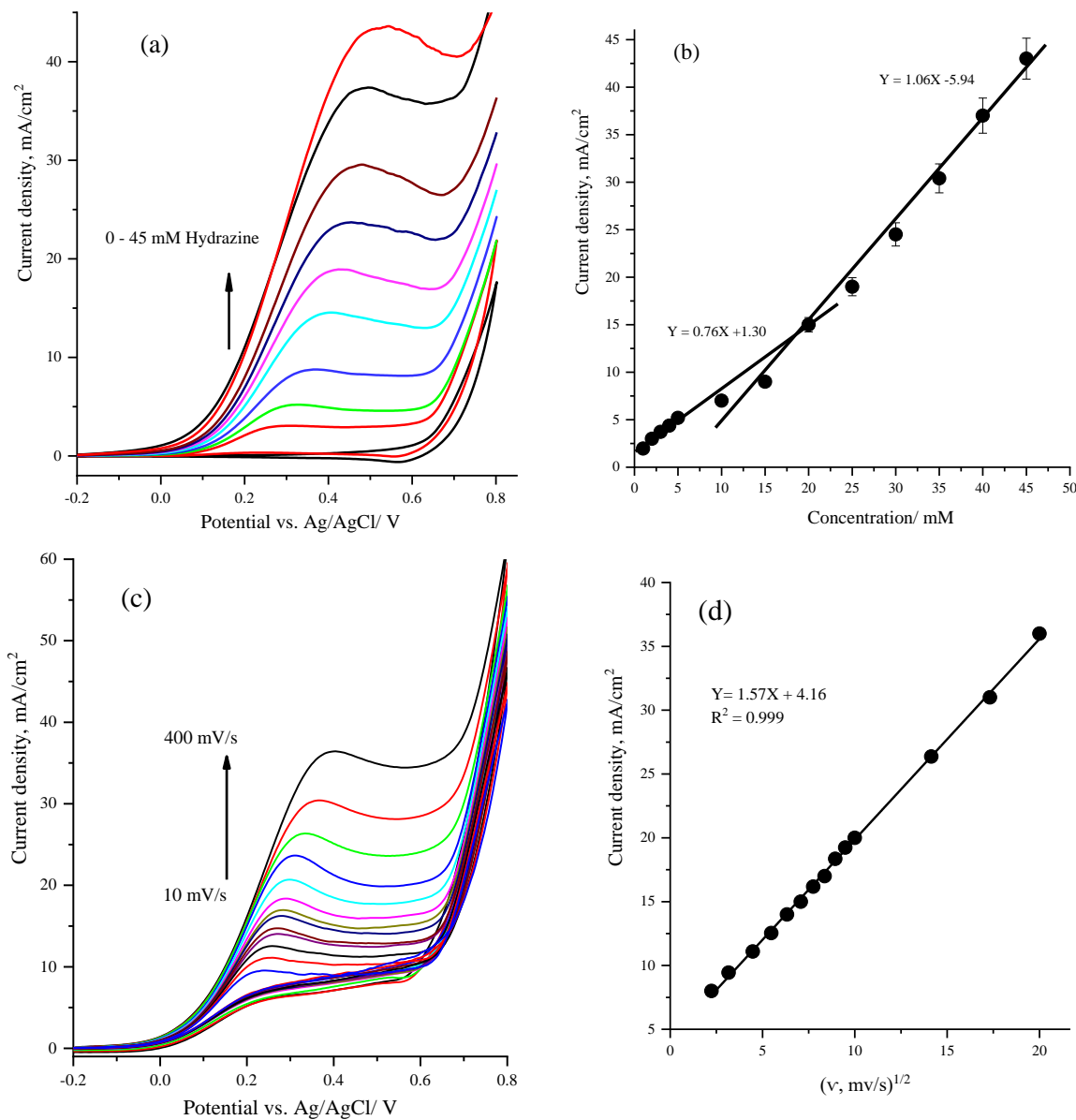


Figure 4. (a) Linear sweep voltammetry at 50 mV/s for the effect of the hydrazine concentration in 1.0 M KOH using 250 μg of the CuO-NS electrode. (b) Correlation between the oxidation peak current and the hydrazine concentration of CuO-NS electrode. (c) Effect of the scan rates of the hydrazine oxidation at the CuO-NS (250 μg) electrode from 10 to 400 mV/s in the 1.0 M KOH solution containing 20.0 mM hydrazine. (d) Relationship of the oxidation peak currents against the square root of the potential scan rates.

The CV results show that the hydrazine anodic oxidation current at the CuO-NS electrode increased with the increase in hydrazine concentration (from 5.0 to 45 mM) accompanied by the peak potential shift to a higher potential from around 0.250 to 0.500 V versus Ag/AgCl as the hydrazine concentration increased. Moreover, the correlation

between the oxidation peak current and the hydrazine concentration showed two regions of the linear range, as shown in Figure 4b. The first region's concentration ranged from 1.0 to 5.0 mM, and the second region's concentration ranged from 10.0 to 45.0 mM with an oxidation current sensitivity of 0.76 mA/cm² mM and 1.06 mA/cm² mM, respectively, indicating a high electrocatalytic activity of CuO-NS towards the hydrazine oxidation because of the nanosheet architecture with a high surface area and the presence of a porous network that facilitated the hydrazine diffusion [60–63]. Moreover, the presence of two dependent linear equations for the correlation between the oxidation peak current and the hydrazine concentration could be related to the variation in the hydrazine/hydroxide ratio and the adsorption competition between hydrazine/hydroxide ions as well as the oxidation mechanism and rate-determining step, in addition to the N₂ gas formation at the catalytic active sites of the CuO-NS catalyst [60–65]. Figure 4c shows the effect of the scan rates of the hydrazine oxidation at the CuO-NS electrode where the CVs were recorded at different potential scan rates from 10 to 400 mV/s in the 1.0 M KOH solution containing 20.0 mM hydrazine. Note that the oxidation peak currents linearly increased against the square root of the potential scan rates ($v^{1/2}$) with the regression equation ($I_{\text{peak}} = 1.57x + 4.16$ and regression coefficient (R^2) = 0.999), as shown in Figure 4d. This behaviour was consistent with the hydrazine oxidation at CuO-NS that occurred via the four-electron transfer and mainly via a diffusion-controlled process [60–63].

To optimize the electrocatalytic sensing activity of the hydrazine oxidation and sensing at the CuO-NS electrode surface, the effects of the applied oxidation potential and the hydroxide electrolyte concentration were investigated using a chronoamperometric technique. Figure 5a shows the chronoamperometry responses of the CuO-NS (250 µg) electrode measured at various applied potentials (from 0.15 to 0.35 V versus Ag/AgCl) to investigate the sensing electroactivity of the CuO-NS electrode towards the successive addition of 1.0 mM hydrazine in the 1.0 M KOH solution and under stirring conditions. In general, the chronoamperometric response of CuO-NS compared with the *bare*-CuO electrodes showed that the oxidation current at all of the applied potentials gradually increased upon the stepwise addition of the hydrazine analyte. The correlation plots between the oxidation current and the hydrazine concentration are shown in Figure 5b, where the oxidation current exhibited a linear response within the studied hydrazine concentration range (from 1.0 to 7.0 mM). The line slopes (hydrazine sensitivity) gradually increased as the applied potential increased and reached a maximum of up to 0.86 mA/cm² mM at the applied potential of 0.30 V versus Ag/AgCl, which was significantly higher than those at the other potentials and approximately eight times higher than those in the case of the *bare*-CuO electrode (slope = 0.10 mA/cm² mM). Therefore, 0.30 V was chosen as the optimum potential in the following experiments for the further quantitative determination of hydrazine.

The electrocatalyst activity of the CuO electrode towards hydrazine oxidation was highly dependent on the OH[−] concentration under the alkali condition [66], and to obtain the optimal hydroxide concentration, Figure 5c shows the effect of the OH[−] concentration on the chronoamperometry profiles of CuO-NS (250 µg) electrode upon the addition of different hydrazine concentrations at an applied potential of 0.30 V versus Ag/AgCl. All of the chronoamperometry curves for the different KOH concentrations exhibited a rapid current increase upon the addition of hydrazine, as shown in Figure 5c. The plots of the hydrazine oxidation current as a function of the hydrazine concentration in the 0.1, 0.5, and 1.0 M KOH solution are shown in Figure 5d. It was observed that in the 1.0 M KOH solution that the CuO-NS electrode displayed the maximum hydrazine sensing performance with a higher sensitivity (0.860 mA/cm²) and linearity, with a high correlation coefficient than in the 0.1 M (0.358 mA/cm²) and 0.5 M (0.594 mA/cm²) KOH solutions. Hence, 1.0 M KOH was used as the optimal solution for hydrazine sensing in this study.

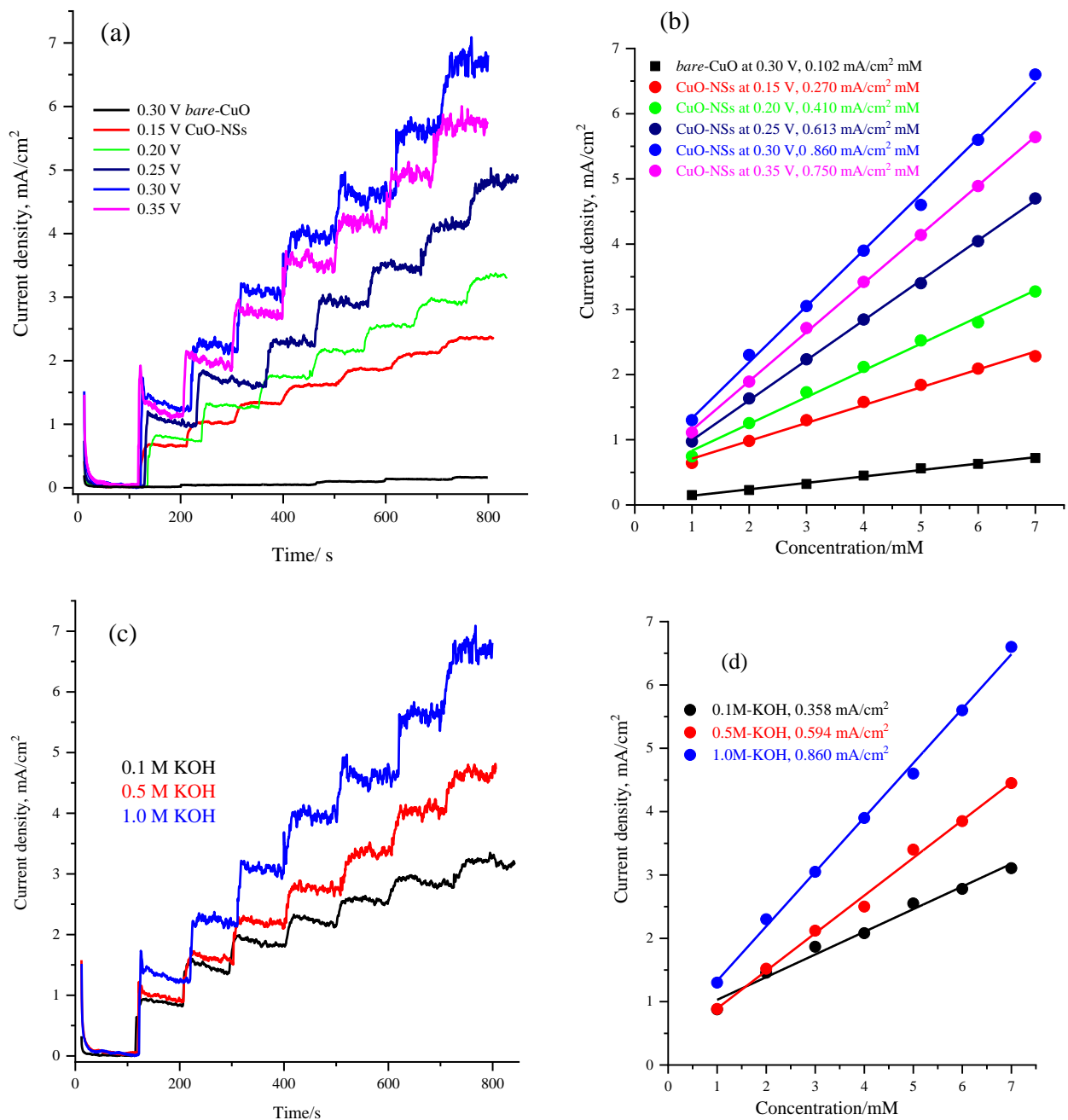


Figure 5. (a) Chronoamperometry responses of the CuO-NS (250 μg) electrode measured at various applied potentials (from 0.15 to 0.35 V vs. Ag/AgCl) after the successive addition of 1.0 mM hydrazine doses in the 1.0 M KOH solution and under a stirring condition. (b) Relationship of the hydrazine oxidation current at various applied potentials against the hydrazine concentration in a range from 1.0 to 7.0 mM. (c) The effect of the KOH concentration on the chronoamperometry profiles of CuO-NS (250 μg) upon the addition of different hydrazine concentrations at an applied potential of 0.30 V versus Ag/AgCl. (d) Plots of the hydrazine oxidation current as a function of the hydrazine concentration in the 0.1, 0.5, and 1.0 M KOH solutions.

The enhanced electrochemical activity of the CuO-NS electrode towards the hydrazine oxidation at various concentrations could be used to achieve high detection sensitivity, relatively wide linear ranges, and a low limit of detection (LOD) of the hydrazine analyte. Figure 6a shows the chronoamperometry response of the CuO-NS compared with *bare*-CuO electrodes at a constant applied potential of 0.30 V and with various injected low concentrations of hydrazine (from 0.025 to 2.5 mM) and under continuous stirring. The

CuO-NS electrode exhibited a significantly larger hydrazine oxidation current and shorter time response of less than 3 s compared with the *bare*-CuO electrode, which indicated the highly enhanced electrocatalytic activity and rapid response time of CuO-NS under the lower concentration of hydrazine. In addition, Figure 6b shows that the CuO-NS sensor displayed more than ten times higher hydrazine sensitivity and a better linear relationship ($1.47 \text{ mA/cm}^2 \text{ mM}$, $R^2 = 0.998$) in the concentration range of 0.25 to 2.5 mM of hydrazine than the *bare*-CuO electrode ($0.11 \text{ mA/cm}^2 \text{ mM}$, $R^2 = 0.996$). The limit of detection (LOD) could be calculated as follows [66]:

$$\text{LOD} = 3 \sigma/S \quad (4)$$

where σ is the background current standard deviation before hydrazine addition and S is the slope of the calibration plot of hydrazine. The achieved limit of detection (LOD) of hydrazine at the CuO-NS electrode reached $15 \mu\text{M}$, which was significantly lower than that of the different nanostructure electrode materials reported in the literature [60–63]. Table 2 summarises the hydrazine sensitivity, linear range, and limit of detection (LOD) for the other electrode materials reported in the literature. The CuO-NS sensor showed a significantly higher sensitivity ($1.47 \text{ mA/cm}^2 \text{ mM}$) and wider linear range from 0.025 to 2.5 mM concentration, which made the CuO-NSs catalyst have the potential to detect a relatively low hydrazine concentration. In addition, the CuO-NS catalyst was easy to fabricate using the one-pot synthesis approach of the foam-surfactant dual template (SFDT) under ambient conditions.

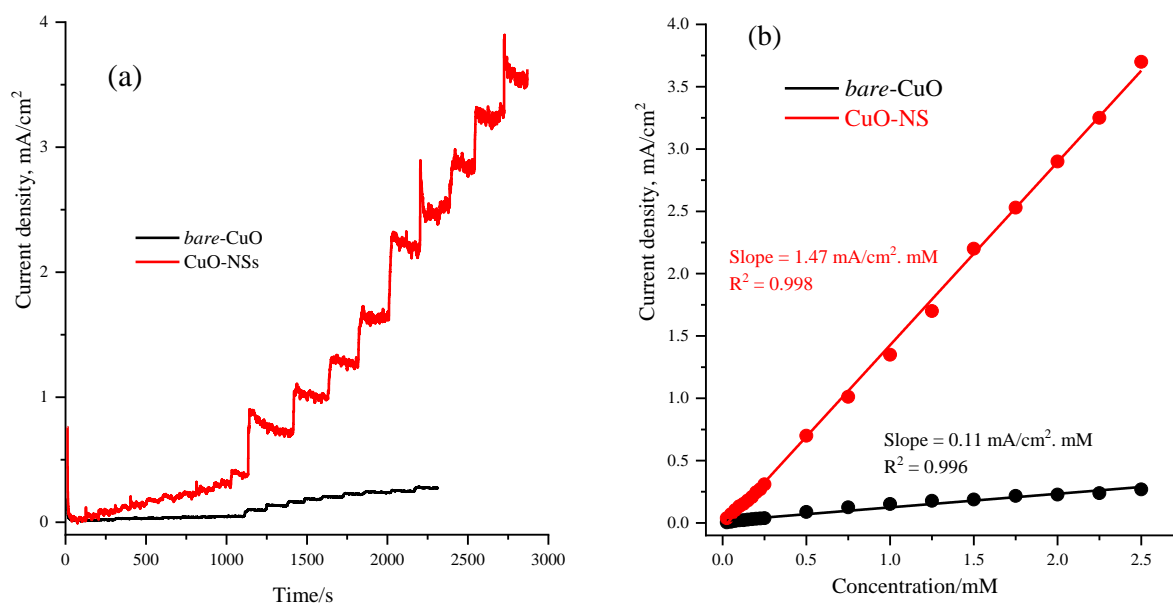


Figure 6. (a) Chronoamperometry curves of the CuO-NS (250 μg) compared with *bare*-CuO electrodes at a constant applied potential of 0.30 V and with various injected low concentrations of hydrazine (from 0.025 to 2.5 mM) and under continuous stirring. (b) Relationship between the hydrazine oxidation current at the CuO-NS electrode and the hydrazine concentration in comparison with the *bare*-CuO electrode.

3.3. Selectivity and Stability of the CuO-NS Sensor

Selectivity is also an important factor for hydrazine sensing; hence, an interference analysis of the CuO-NS electrode towards various interferences was conducted using chronoamperometry at the applied potential of 0.30 V versus Ag/AgCl, as shown in Figure 7a. The selectivity of the CuO-NS electrode was measured with the addition of a 10 mM solution of each of the common interferences considered, such as uric acid, urea, cysteine, and NaCl. In this context, a solution of 1.0 M KOH was initially used, followed

by the successive addition of 1, 2, and 4 mM hydrazine, and then a 10 mM concentration of the interference of uric acid, urea, cysteine, and NaCl were stepwise added to the test solution under continuous magnetic stirring. It was seen that the initial addition of the hydrazine doses led to a substantial current increase, while the stepwise additions of the interferences of uric acid, urea, cysteine, and NaCl produced almost negligible current responses. Moreover, the further stepwise addition of 1, 2, and 4 mM hydrazine produced a current response enhancement similar to that obtained during the first-time addition of hydrazine, implying that the electrode showed excellent selectivity for hydrazine detection. For the hydrazine electrochemical oxidation stability and efficiency study at the CuO-NS electrode, Figure 7b shows the current–time signal response during prolonged oxidation at an applied potential of 0.30 V versus Ag/AgCl and after the successive addition of 5.0 mM and 10 mM hydrazine to 1.0 M KOH under magnetic stirring. The results show that the oxidation current density signal was extremely stable for more than 1.0 h with a negligible current change observed upon the addition of either the low (5.0 mM) or the high (10.0 mM) concentration regime of hydrazine.

Table 2. Compared performances of different types of electrode material for hydrazine sensitivity, linear range, and limit of detection.

Electrode Material	Applied Potential (V)	Sensitivity ($\mu\text{A}/\text{cm}^2 \text{ mM}$)	Linear Range (μM)	The Detection Limit (μM)	Reference
CoOOH nanosheets		155	20–1200	20	[67]
ZnO NRs/Ag	-	~105	0.01–98.6	-	[68]
ZnCo ₂ O ₄	0.55	~0.5	100–600	0.2	[14]
CuO/OMC–GCE	-	537	1–2.11 $\times 10^3$	0.887	[18]
CuO/GCE	-	~94	0.1–600	0.03	[50]
CuO/CNTs-rGO/GCE	0.45	~4.0	1.2–430	0.2	[69]
CuO NA/ GCE	0.0	~30	0.2–20	0.17	[62]
Cu ₂ O-nanoarray	0.0358	~0.02	0.1–1221	0.15	[60]
Nano-CuO modified GCE	-	~8.0	50–2500	12	[63]
CuO-NSs/CP	0.30	1470	25–2500	15	This work

Figure 7c shows the long-term stability of the CuO-NS catalyst during storage for 30 days in the air, as investigated every 10 days, by the chronoamperometric response to the hydrazine successive stepwise addition from 1.0 to 7.0 mM in the 1.0 M KOH electrolyte under magnetic stirring and using a 250 μg loading of the CuO-NS catalyst. As shown in Figure 7c, the CuO-NS electrode exhibited a very stable hydrazine oxidation current with almost no change in the hydrazine sensitivity (average sensitivity of 0.87 $\text{mA}/\text{cm}^2 \text{ mM}$) during frequent usage for 30 days and storage in air, as shown in the inset in Figure 7c, which confirmed the high stability behaviour of the CuO-NS electrode during the sensing of hydrazine.

3.4. Electrochemical Analysis of Real Samples

Next, the feasibility of the CuO-NS electrode in a real tap water sample for hydrazine sensing collected from Riyadh and bottled drinking water supplied by Nova Company was evaluated. The chronoamperometric response of the CuO-NS electrode (250 μg loading) towards the hydrazine oxidation was observed with the successive stepwise addition of 1.0 mM hydrazine to 50 mL of the 1.0 M KOH solution containing 5.0 mL from an unknown concentration of the real samples and under magnetic stirring. The recovery experiments were carried out through the standard addition method for the amperometry current response at various concentrations of hydrazine in the real samples. As shown in Table S1 (Supporting Information), the recovery results were in the range of 97–108% for

tap water and 99–106% for bottled drinking water, indicating that the CuO-NS electrode is a promising electrode for hydrazine determination in real samples.

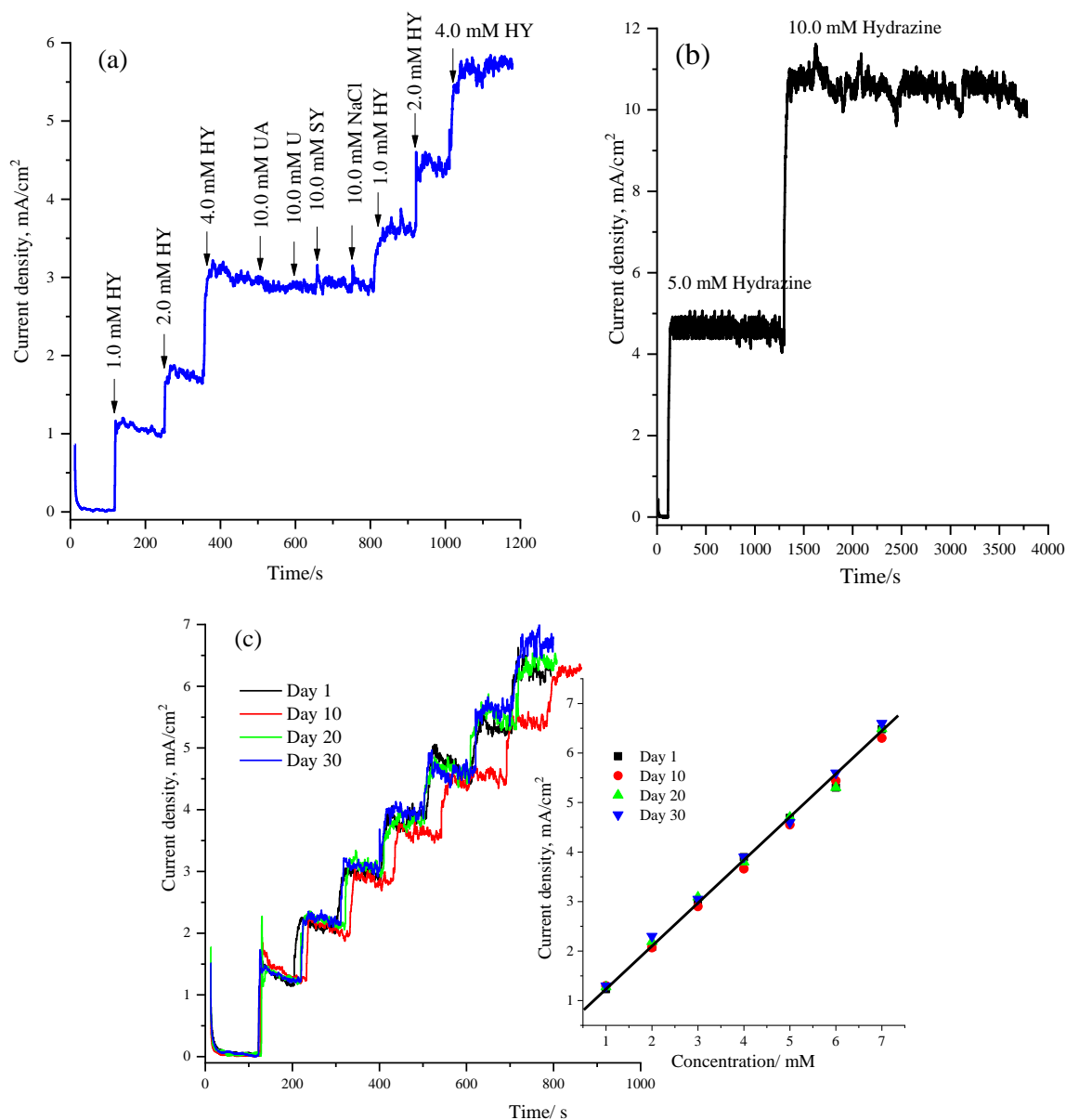


Figure 7. (a) Chronoamperometry response of the CuO-NS (250 μ g) electrode at an applied potential of 0.30 V vs. Ag/AgCl and after the addition of 10 mM solution of uric acid, urea, cysteine, or NaCl interference and in the presence of 1, 2, or 4 mM hydrazine in 1.0 M KOH solution. (b) Chronoamperometry signal response of the CuO-NS (250 μ g) electrode at an applied potential of 0.30 V vs. Ag/AgCl during a prolonged oxidation period and after the successive addition of 5.0 mM and 10 mM hydrazine to 1.0 M KOH under magnetic stirring. (c) Long-term chronoamperometry curves of the CuO-NS catalyst after storage in air for 30 days, as investigated every 10 days, to hydrazine oxidation through the successive stepwise addition of 1.0 to 7.0 mM hydrazine in the 1.0 M KOH electrolyte and under continuous magnetic stirring, the inset shows the correlation between the hydrazine oxidation current density and the concentration over 30 days of usage and store.

4. Conclusions

In summary, a nanosheet architecture of the copper oxide (CuO-NS) electrocatalyst was obtained at room temperature via a versatile one-pot foam-surfactant dual template (SFDT) synthesis approach using sodium borohydride (NaBH_4) as a reducing agent. NaBH_4

chemically reduced the copper ions confined in the aqueous domain of the Brij[®]58 surfactant template, as well as in situ generating excessive hydrogen foam that exfoliate the deposited copper oxide nanosheets. The as-prepared CuO-NS electrode exhibited a remarkably enhanced electrocatalytic activity and sensitivity, low detection limit, and excellent selectivity and stability towards hydrazine oxidation in an alkaline solution. The electrochemical CuO-NS sensing activity for hydrazine oxidation revealed that the CuO nanosheets had a superior sensing performance compared with the bare-CuO and reported state-of-the-art catalysts due to the nanosheet architecture and active sites' high surface area, which facilitated the charge transfer as well as the mass transport diffusion of the hydrazine molecule. In addition, hydrazine detection in tap and bottled water using CuO-NS electrodes was achieved with a good recovery, which confirmed the potential of CuO-NS electrodes for practical use. The foam-surfactant dual template (SFDT) is a one-pot synthesis approach that could be applied to produce a wide range of nanomaterials with various compositions and nanoarchitectures at room temperature for enhancing electrochemical catalytic reactions.

Supplementary Materials: The following supporting information can be downloaded at: <https://www.mdpi.com/article/10.3390/nano13010129/s1>. Figure S1: XRD of CuO-NSs and bare-CuO. Figure S2: The XPS survey spectrum of the as-prepared CuO-NS. Figure S3: (a) SAED pattern of the CuO nanosheets and (b) TEM image of the bare-CuO catalyst deposited in the absence of the surfactant. Table S1: Results for detection of hydrazine from different water sources injected with a known concentration of hydrazine.

Author Contributions: M.A.G. proposed the conceptualization plan, wrote the results and discussion, and reviewed and submitted the final manuscript; E.M.A. performed the experimental work and electrochemical characterisation and wrote the original draft; A.A.-W. provided the resources and supervised the whole project; M.K. carried out the catalyst XRD and BET analysis; S.F.A. analysed and wrote the crystal structure part. All authors have read and agreed to the published version of the manuscript.

Funding: This research was funded by King Saud University, Riyadh, Saudi Arabia, RSP-2022R518.

Data Availability Statement: Not applicable.

Acknowledgments: The authors would like to express their sincere gratitude to the researchers supporting Project number (RSP-2022R518), King Saud University, Riyadh, Saudi Arabia.

Conflicts of Interest: The authors declare no conflict of interest.

References

1. Zhang, X.Y.; Yang, Y.S.; Wang, W.; Jiao, Q.C.; Zhu, H.L. Fluorescent sensors for the detection of hydrazine in environmental and biological systems: Recent advances and future prospects. *Coord. Chem. Rev.* **2020**, *417*, 213367. [[CrossRef](#)]
2. Hwang, H.; Hong, S.; Kim, D.H.; Kang, M.S.; Park, J.S.; Uhm, S.; Lee, J. Optimistic performance of carbon-free hydrazine fuel cells based on controlled electrode structure and water management. *J. Energy Chem.* **2020**, *51*, 175–181. [[CrossRef](#)]
3. Nufer, B. *A Summary of NASA and USAF Hypergolic Propellant Related Spills and Fires*; NASA Kennedy Space Center, Mail Stop: Washington, DC, USA, 2010; p. 1994.
4. Yadav, M.; Sharma, D.; Sarkar, T.K. Adsorption and corrosion inhibitive properties of synthesized hydrazine compounds on N80 steel/hydrochloric acid interface: Electrochemical and DFT studies. *J. Mol. Liq.* **2015**, *212*, 451–460. [[CrossRef](#)]
5. Crisafulli, R.; de Barros, V.V.S.; de Oliveira, F.E.R.; de Araújo Rocha, T.; Zignani, S.; Spadaro, L.; Palella, A.; Dias, J.; Linares, J.J. On the promotional effect of Cu on Pt for hydrazine electrooxidation in alkaline medium. *Appl. Catal. B Environ.* **2018**, *236*, 36–44. [[CrossRef](#)]
6. Umar, A.; Akhtar, M.S.; Al-Hajry, A.; Al-Assiri, M.S.; Dar, G.N.; Islam, M.S. Enhanced photocatalytic degradation of harmful dye and phenyl hydrazine chemical sensing using ZnO nanourchins. *Chem. Eng. J.* **2015**, *262*, 588–596. [[CrossRef](#)]
7. Vidrio, H.; Fernández, G.; Medina, M.; Alvarez, E.; Orallo, F. Effects of hydrazine derivatives on vascular smooth muscle contractility, blood pressure and cGMP production in rats: Comparison with hydralazine. *Vasc. Pharmacol.* **2003**, *40*, 13–21. [[CrossRef](#)]
8. Bharate, S.S. Critical analysis of drug product recalls due to nitrosamine impurities. *J. Med. Chem.* **2021**, *64*, 2923–2936. [[CrossRef](#)]

9. Zhong, L.; Zhang, X.; Tang, C.; Chen, Y.; Shen, T.; Zhu, C.; Ying, H. Hydrazine hydrate and organosolv synergetic pretreatment of corn stover to enhance enzymatic saccharification and co-production of high-quality antioxidant lignin. *Bioresour. Technol.* **2018**, *268*, 677–683. [[CrossRef](#)]
10. Mokhtari, N.; Khataei, M.M.; Dinari, M.; Monjezi, B.H.; Yamini, Y.; Hatami, M. Solid-phase extraction and microextraction of chlorophenols and triazine herbicides with a novel hydrazone-based covalent triazine polymer as the adsorbent. *Microchem. J.* **2021**, *160*, 105634. [[CrossRef](#)]
11. Wang, Z.; Zhang, Y.; Meng, Z.; Li, M.; Zhang, C.; Yang, L.; Xu, X.; Wang, S. Development of a ratiometric fluorescent probe with large Stokes shift and emission wavelength shift for real-time tracking of hydrazine and its multiple applications in environmental analysis and biological imaging. *J. Hazard. Mater.* **2022**, *422*, 126891. [[CrossRef](#)]
12. Spencer, P.S.; Kisby, G.E. Role of hydrazine-related chemicals in cancer and neurodegenerative disease. *Chem. Res. Toxicol.* **2021**, *34*, 1953–1969. [[CrossRef](#)] [[PubMed](#)]
13. Song, Y.; Chen, G.; Han, X.; You, J.; Yu, F. A highly sensitive near-infrared ratiometric fluorescent probe for imaging of mitochondrial hydrazine in cells and in mice models. *Sens. Actuators B Chem.* **2019**, *286*, 69–76. [[CrossRef](#)]
14. Pathak, A.; Gupta, B.D. Palladium nanoparticles embedded PPy shell coated CNTs towards a high performance hydrazine detection through optical fiber plasmonic sensor. *Sens. Actuators B Chem.* **2021**, *326*, 128717. [[CrossRef](#)]
15. Oh, J.A.; Shin, H.S. Simple determination of hydrazine in waste water by headspace solid-phase micro extraction and gas chromatography-tandem mass spectrometry after derivatization with trifluoro pentanedione. *Anal. Chim. Acta* **2017**, *950*, 57–63. [[CrossRef](#)] [[PubMed](#)]
16. Zhang, W.; Huo, F.; Liu, T.; Yin, C. Ratiometric fluorescence probe for hydrazine vapor detection and biological imaging. *J. Mater. Chem. B* **2018**, *6*, 8085–8089. [[CrossRef](#)]
17. Liu, J.; Jiang, J.; Dou, Y.; Zhang, F.; Liu, X.; Qu, J.; Zhu, Q. A novel chemiluminescent probe for hydrazine detection in water and HeLa cells. *Org. Biomol. Chem.* **2019**, *17*, 6975–6979. [[CrossRef](#)]
18. Omar, F.S.; Numan, A.; Duraisamy, N.; Bashir, S.; Ramesh, K.; Ramesh, S. A promising binary nanocomposite of zinc cobaltite intercalated with polyaniline for supercapacitor and hydrazine sensor. *J. Alloys Compound.* **2017**, *716*, 96–105. [[CrossRef](#)]
19. Nemakal, M.; Aralekallu, S.; Mohammed, I.; Swamy, S.; Sannegowda, L.K. Electropolymerized octabenzimidazole phthalocyanine as an amperometric sensor for hydrazine. *J. Electroanal. Chem.* **2019**, *839*, 238–246. [[CrossRef](#)]
20. Gholivand, M.B.; Azadbakht, A. A novel hydrazine electrochemical sensor based on a zirconium hexacyanoferrate film-bimetallic Au–Pt inorganic–organic hybrid nanocomposite onto glassy carbon-modified electrode. *Electrochim. Acta* **2011**, *56*, 10044–10054. [[CrossRef](#)]
21. Saeb, E.; Asadpour-Zeynali, K. Facile synthesis of TiO₂@PANI@Au nanocomposite as an electrochemical sensor for determination of hydrazine. *Microchem. J.* **2021**, *160*, 105603. [[CrossRef](#)]
22. Wang, L.; Meng, T.; Jia, H.; Feng, Y.; Gong, T.; Wang, H.; Zhang, Y. Electrochemical study of hydrazine oxidation by leaf-shaped copper oxide loaded on highly ordered mesoporous carbon composite. *J. Colloid Interface Sci.* **2019**, *549*, 98–104. [[CrossRef](#)] [[PubMed](#)]
23. Mahmoudian, M.R.; Basirun, W.J.; Woi, P.M.; Sookhajian, M.; Yousefi, R.; Ghadimi, H.; Alias, Y. Synthesis and characterization of Co₃O₄ ultra-nanosheets and Co₃O₄ ultra-nanosheet-Ni(OH)₂ as non-enzymatic electrochemical sensors for glucose detection. *Mater. Sci. Eng. C* **2016**, *59*, 500–508. [[CrossRef](#)] [[PubMed](#)]
24. Shinde, S.; Dhaygude, H.; Kim, D.Y.; Ghodake, G.; Bhagwat, P.; Dandge, P.; Fulari, V. Improved synthesis of copper oxide nanosheets and its application in development of supercapacitor and antimicrobial agents. *J. Ind. Eng. Chem.* **2016**, *36*, 116–120. [[CrossRef](#)]
25. Kamali, M.; Samari, F.; Sedaghati, F. Low-temperature phyto-synthesis of copper oxide nanosheets: Its catalytic effect and application for colorimetric sensing. *Mater. Sci. Eng. C* **2019**, *103*, 109744. [[CrossRef](#)] [[PubMed](#)]
26. Bhattacharjee, A.; Ahmaruzzaman, M. CuO nanostructures: Facile synthesis and applications for enhanced photodegradation of organic compounds and reduction of p-nitrophenol from aqueous phase. *RSC Adv.* **2016**, *6*, 41348–41363. [[CrossRef](#)]
27. Sundar, S.; Venkatachalam, G.; Kwon, S.J. Biosynthesis of copper oxide (CuO) nanowires and their use for the electrochemical sensing of dopamine. *Nanomaterials* **2018**, *8*, 823. [[CrossRef](#)]
28. Rutkowska, I.A.; Wadas, A.; Szaniawska, E.; Chmielnicka, A.; Zlotorowicz, A.; Kulesza, P.J. Elucidation of activity of copper and copper oxide nanomaterials for electrocatalytic and photoelectrochemical reduction of carbon dioxide. *Curr. Opin. Electrochem.* **2020**, *23*, 131–138. [[CrossRef](#)]
29. Akintelu, S.A.; Folorunso, A.S.; Folorunso, F.A.; Oyebamiji, A.K. Green synthesis of copper oxide nanoparticles for biomedical application and environmental remediation. *Heliyon* **2020**, *6*, e04508. [[CrossRef](#)]
30. Montgomery, M.J.; Sugak, N.V.; Yang, K.R.; Rogers, J.M.; Kube, S.A.; Ratnov, A.C.; Schroers, J.; Batista, V.S.; Pfefferle, L.D. Semiconductor-to-conductor transition in 2D copper (ii) oxide nanosheets through surface sulfur-functionalization. *Nanoscale* **2020**, *12*, 14549–14559. [[CrossRef](#)]
31. Vinothkumar, P.; Manoharan, C.; Shanmugapriya, B.; Bououdina, M. Effect of reaction time on structural, morphological, optical and photocatalytic properties of copper oxide (CuO) nanostructures. *J. Mater. Sci. Mater. Electron.* **2019**, *30*, 6249–6262. [[CrossRef](#)]
32. Li, R.; Liu, X.; Wang, H.; Wu, Y.; Chan, K.C.; Lu, Z. Sandwich nanoporous framework decorated with vertical CuO nanowire arrays for electrochemical glucose sensing. *Electrochim. Acta* **2019**, *299*, 470–478. [[CrossRef](#)]

33. Chavali, M.S.; Nikolova, M.P. Metal oxide nanoparticles and their applications in nanotechnology. *SN Appl. Sci.* **2019**, *1*, 607. [[CrossRef](#)]
34. Yadav, A.A.; Hunge, Y.M.; Kang, S.-W. Chemical synthesis of a microsphere-like copper molybdate electrode for oxygen evolution reaction. *Surf. Interfaces* **2021**, *26*, 101425. [[CrossRef](#)]
35. Yadav, A.A.; Hunge, Y.M.; Kang, S.-W. Spongy ball-like copper oxide nanostructure modified by reduced graphene oxide for enhanced photocatalytic hydrogen production. *Mater. Res. Bull.* **2021**, *133*, 111026. [[CrossRef](#)]
36. Hosseini, S.R.; Kamali-Rousta, M. Preparation of electro-spun CuO nanoparticle and its application for hydrazine hydrate electro-oxidation. *Electrochim. Acta* **2016**, *189*, 45–53. [[CrossRef](#)]
37. Kulkarni, S.; Ghosh, R. A simple approach for sensing and accurate prediction of multiple organic vapors by sensors based on CuO nanowires. *Sens. Actuators B Chem.* **2021**, *335*, 129701. [[CrossRef](#)]
38. Bai, H.; Guo, H.; Wang, J.; Dong, Y.; Liu, B.; Xie, Z.; Guo, F.; Chen, D.; Zhang, R.; Zheng, Y. A room-temperature NO₂ gas sensor based on CuO nanoflakes modified with rGO nanosheets. *Sens. Actuators B Chem.* **2021**, *337*, 129783. [[CrossRef](#)]
39. Kong, C.; Lv, J.; Hu, X.; Zhao, N.; Liu, K.; Zhang, X.; Meng, G.; Yang, Z.; Yang, S. Template-synthesis of hierarchical CuO nanoflowers constructed by ultrathin nanosheets and their application for non-enzymatic glucose detection. *Mater. Lett.* **2018**, *219*, 134–137. [[CrossRef](#)]
40. Ghosh, A.; Miah, M.; Bera, A.; Saha, S.K.; Ghosh, B. Synthesis of freestanding 2D CuO nanosheets at room temperature through a simple surfactant free co-precipitation process and its application as electrode material in supercapacitors. *J. Alloys Compound.* **2021**, *862*, 158549. [[CrossRef](#)]
41. Kim, R.; Jang, J.S.; Kim, D.H.; Kang, J.Y.; Cho, H.J.; Jeong, Y.J.; Kim, I.D. A general synthesis of crumpled metal oxide nanosheets as superior chemiresistive sensing layers. *Adv. Funct. Mater.* **2019**, *29*, 1903128. [[CrossRef](#)]
42. Gunjekar, J.L.; Kim, I.Y.; Lee, J.M.; Jo, Y.K.; Hwang, S.J. Exploration of nanostructured functional materials based on hybridization of inorganic 2D nanosheets. *J. Phys. Chem. C* **2014**, *118*, 3847–3863. [[CrossRef](#)]
43. Zhu, G.; Xu, H.; Xiao, Y.; Liu, Y.; Yuan, A.; Shen, X. Facile fabrication and enhanced sensing properties of hierarchically porous CuO architectures. *ACS Appl. Mater. Interfaces* **2012**, *4*, 744–751. [[CrossRef](#)] [[PubMed](#)]
44. Umar, A.; Ibrahim, A.A.; Ammar, H.Y.; Nakate, U.T.; Albargi, H.B.; Hahn, Y.B. Urchin like CuO hollow microspheres for selective high response ethanol sensor application: Experimental and theoretical studies. *Ceram. Int.* **2021**, *47*, 12084–12095. [[CrossRef](#)]
45. Sun, F.; Zhu, R.; Jiang, H.; Huang, H.; Liu, P.; Zheng, Y. Synthesis of Novel CuO Nanosheets with Porous Structure and Their Non-Enzymatic Glucose Sensing Applications. *Electroanalysis* **2015**, *27*, 1238–1244. [[CrossRef](#)]
46. Zhu, Y.; Xu, Z.; Yan, K.; Zhao, H.; Zhang, J. One-step synthesis of CuO–Cu₂O heterojunction by flame spray pyrolysis for cathodic photoelectrochemical sensing of l-cysteine. *ACS Appl. Mater. Interfaces* **2017**, *9*, 40452–40460. [[CrossRef](#)]
47. Foroughi, F.; Rahsepar, M.; Hadianfard, M.J.; Kim, H. Microwave-assisted synthesis of graphene modified CuO nanoparticles for voltammetric enzyme-free sensing of glucose at biological pH values. *Microchim. Acta* **2018**, *185*, 57. [[CrossRef](#)] [[PubMed](#)]
48. Heo, S.G.; Yang, W.S.; Kim, S.; Park, Y.M.; Park, K.T.; Oh, S.J.; Seo, S.J. Synthesis, characterization and non-enzymatic lactate sensing performance investigation of mesoporous copper oxide (CuO) using inverse micelle method. *Appl Surf. Sci.* **2021**, *555*, 149638. [[CrossRef](#)]
49. Das, G.; Tran, T.Q.N.; Yoon, H.H. Spherulitic copper–copper oxide nanostructure-based highly sensitive nonenzymatic glucose sensor. *Int. J. Nanomed.* **2015**, *10*, 165. [[CrossRef](#)]
50. Zhang, P.; He, T.; Li, P.; Zeng, X.; Huang, Y. New insight into the hierarchical microsphere evolution of organic three-dimensional layer double hydroxide: The key role of the surfactant template. *Langmuir* **2019**, *35*, 13562–13569. [[CrossRef](#)]
51. Almutairi, E.M.; Ghanem, M.A.; Al-Warthan, A.; Shaik, M.R.; Adil, S.F. Chemical deposition and exfoliation from liquid crystal template: Nickel / nickel (II) hydroxide nanoflakes electrocatalyst for a non-enzymatic glucose oxidation reaction. *Arab. J. Chem.* **2022**, *15*, 103467. [[CrossRef](#)]
52. Poolakkandy, R.R.; Menampambath, M.M. Soft-template-assisted synthesis: A promising approach for the fabrication of transition metal oxides. *Nanoscale Adv.* **2020**, *2*, 5015–5045. [[CrossRef](#)] [[PubMed](#)]
53. Al-Sharif, M.S.; Arunachalam, P.; Abiti, T.; Amer, M.S.; Al-Shalwi, M.; Ghanem, M.A. Mesoporous cobalt phosphate electrocatalyst prepared using liquid crystal template for methanol oxidation reaction in alkaline solution. *Arab. J. Chem.* **2020**, *13*, 2873–2882. [[CrossRef](#)]
54. Song, T.; Gao, F.; Guo, S.; Zhang, Y.; Li, S.; You, H.; Du, Y. A review of the role and mechanism of surfactants in the morphology control of metal nanoparticles. *Nanoscale* **2021**, *13*, 3895–3910. [[CrossRef](#)] [[PubMed](#)]
55. Bamuqaddam, A.M.; Aladeemy, S.A.; Ghanem, M.A.; Al-Mayouf, A.M.; Alotaibi, N.H.; Marken, F. Foam Synthesis of Nickel/Nickel (II) Hydroxide Nanoflakes Using Double Templates of Surfactant Liquid Crystal and Hydrogen Bubbles: A High-Performance Catalyst for Methanol Electrooxidation in Alkaline Solution. *Nanomaterials* **2022**, *12*, 879. [[CrossRef](#)] [[PubMed](#)]
56. Naikoo, G.A.; Dar, R.A.; Khan, F. Hierarchically macro/mesostructured porous copper oxide: Facile synthesis, characterization, catalytic performance and electrochemical study of mesoporous copper oxide monoliths. *J. Mater. Chem. A* **2014**, *2*, 11792–11798. [[CrossRef](#)]
57. Sing, K.S.W.; Everett, D.H.; Haul, R.A.W.; Moscou, L.; Pierotti, R.A.; Rouquerol, J.; Siemieniewska, T. Reporting physisorption data for gas/solid systems with special reference to the determination of surface area and porosity. *Pure Appl. Chem.* **1985**, *57*, 603–619. [[CrossRef](#)]

58. Vasquez, R.P. CuO by XPS. *Surf. Sci. Spectra* **1998**, *5*, 262–266. [[CrossRef](#)]
59. Lv, W.; Li, L.; Meng, Q.; Zhang, X. Molybdenum-doped CuO nanosheets on Ni foams with extraordinary specific capacitance for advanced hybrid supercapacitors. *J. Mater. Sci.* **2020**, *55*, 2492–2502. [[CrossRef](#)]
60. Wang, G.; Gu, A.; Wang, W.; Wei, Y.; Wu, J.; Wang, G.; Zhang, X.; Fang, B. Copper oxide nanoarray based on the substrate of Cu applied for the chemical sensor of hydrazine detection. *Electrochem. Commun.* **2009**, *11*, 631–634. [[CrossRef](#)]
61. Jia, Y.; Shang, N.; He, X.; Nsabimana, A.; Gao, Y.; Ju, J.; Yang, X.; Zhang, Y. Electrocatalytically active cuprous oxide nanocubes anchored onto macroporous carbon composite for hydrazine detection. *J. Colloid Interface Sci.* **2022**, *606*, 1239–1248. [[CrossRef](#)]
62. Yin, Z.; Liu, L.; Yang, Z. An amperometric sensor for hydrazine based on nano-copper oxide modified electrode. *J. Solid State Electrochem.* **2011**, *15*, 821–827. [[CrossRef](#)]
63. Raoof, J.B.; Ojani, R.; Jamali, F.; Hosseini, S.R. Electrochemical detection of hydrazine using a copper oxide nanoparticle modified glassy carbon electrode. *Caspian J. Chem.* **2012**, *1*, 73–85.
64. Karim-Nezhad, G.; Jafarloo, R.; Dorraji, P.S. Copper (hydr) oxide modified copper electrode for electrocatalytic oxidation of hydrazine in alkaline media. *Electrochim. Acta* **2009**, *54*, 5721–5726. [[CrossRef](#)]
65. Jia, F.; Zhao, J.; Yu, X. Nanoporous Cu film/Cu plate with superior catalytic performance toward electro-oxidation of hydrazine. *J. Power Sources* **2013**, *222*, 135–139. [[CrossRef](#)]
66. Li, H.; Zhang, L.; Mao, Y.; Wen, C.; Zhao, P. A simple electrochemical route to access amorphous Co-Ni hydroxide for non-enzymatic glucose sensing. *Nanoscale Res. Lett.* **2019**, *14*, 135. [[CrossRef](#)]
67. Lee, K.K.; Loh, P.Y.; Sow, C.H.; Chin, W.S. CoOOH nanosheet electrodes: Simple fabrication for sensitive electrochemical sensing of hydrogen peroxide and hydrazine. *Biosens. Bioelectron.* **2013**, *39*, 255–260. [[CrossRef](#)] [[PubMed](#)]
68. Ahmad, R.; Tripathy, N.; Ahn, M.S.; Hahn, Y.B. Highly stable hydrazine chemical sensor based on vertically-aligned ZnO nanorods grown on electrode. *J. Colloid Interface Sci.* **2017**, *494*, 153–158. [[CrossRef](#)] [[PubMed](#)]
69. Zhao, Z.; Wang, W.; Tang, W.; Xie, Y.; Li, Y.; Song, J.; Zhuiykov, S.; Gong, W. Synthesis and electrochemistry performance of CuO-functionalized CNTs-rGO nanocomposites for highly sensitive hydrazine detection. *Ionics* **2020**, *26*, 2599–2609. [[CrossRef](#)]

Disclaimer/Publisher’s Note: The statements, opinions and data contained in all publications are solely those of the individual author(s) and contributor(s) and not of MDPI and/or the editor(s). MDPI and/or the editor(s) disclaim responsibility for any injury to people or property resulting from any ideas, methods, instructions or products referred to in the content.